

THE DYNAMICS OF A COLLAPSING POLYELECTROLYTE GEL*

GIULIA L. CELORA[†], MATTHEW G. HENNESSY[†], ANDREAS MÜNCH[†],
BARBARA WAGNER[‡], AND SARAH L. WATERS[†]

Abstract. We analyse the dynamics of different routes to collapse of a constrained polyelectrolyte gel in contact with an ionic bath. The evolution of the gel is described by a model that incorporates non-linear elasticity, Stefan-Maxwell diffusion and interfacial gradient free energy to account for phase separation of the gel. A bifurcation analysis of the homogeneous equilibrium states reveals three solution branches at low ion concentrations in the bath, giving way to only one above a critical ion concentration. We present numerical solutions that capture both the spatial heterogeneity and the multiple time-scales involved in the process of collapse. These solutions are complemented by two analytical studies. Firstly, a phase-plane analysis that reveals the existence of a depletion front for the transition from the highly swollen to the new collapsed equilibrium state. This depletion front is initiated after the fast ionic diffusion has set the initial condition for this time regime. Secondly, we perform a linear stability analysis about the homogeneous states that show that for a range of ion concentrations in the bath, spinodal decomposition of the swollen state gives rise to localized solvent-rich (poor) and, due to the electro-neutrality condition, ion-poor (rich) phases that coarsen on the route to collapse. This dynamics of a collapsing polyelectrolyte gel has not been described before.

Key words. polyelectrolyte gel, collapse, phase-space analysis, spinodal decomposition, stability analysis

AMS subject classifications. 74N20, 74F10, 35B35

1. Introduction. Ever since the seminal papers by Tanaka et al. [38] and Dusek [12], research on swelling and collapse of polyelectrolyte gels has been very intensive, both theoretically and experimentally [8, 7, 18, 27, 29]. These systems, combining elements of electrochemistry and condensed matter physics, display intriguing and subtle properties motivating both experimental and theoretical studies to understand their rich behaviour. These gels also have a wealth of technological applications, and a better understanding of polyelectrolyte gels serves as a basis for developing smart, responsive materials and sensors [2, 5, 16, 37], for example. In particular, research in this field is driven by applications in medicine [16, 23], e.g. for drug delivery and tissue engineering. Additionally, polyelectrolyte gels are used as a model system for many types of biological tissues [25, 30], or in the modelling of mucus [24, 36], to gain fundamental insight into diverse phenomena in biology. Polyelectrolytes also serve as a model for bio-macromolecules such as DNA and RNA [13, 32, 41].

In its simplest form a polyelectrolyte gel is a network of covalently cross-linked polyelectrolyte macromolecules, that is, of polymer chains carrying fixed charges of the same sign, immersed in a solvent. If placed in an ionic bath, the gel will approach a new equilibrium state driven by osmotic effects and will swell or shrink [18]. This process depends on factors such as the concentration and valency of the salt in the solvent, the (nonlinear) elasticity of the gel, the concentration of fixed charges and the number of ionizable groups of the polyelectrolyte macromolecule, as well external fields such as an applied electric field or the temperature [22]. The change in volume

*Submitted to the editors DATE.

Funding: Funding Contract Number xxxx

[†]Mathematical Institute, Woodstock Road, University of Oxford, Oxford, OX2 6GG, UK (celora@maths.ox.ac.uk, hennessy@maths.ox.ac.uk, muench@maths.ox.ac.uk, waters@maths.ox.ac.uk)

[‡]Weierstrass Institute, Mohrenstrasse 39, 10117 Berlin, Germany (wagnerb@wias-berlin.de)

does not always proceed continuously [1, 29, 40]. The discontinuous volume phase transition typically considers a gel that is divided into co-existing subdomains that are in thermodynamic equilibrium with jump conditions imposed at their interfaces [9, 3].

Unlike non-ionic hydrogels [15, 33, 39], subtle changes in the environment surrounding the gel such as increasing the ion concentration can have a dramatic effect and result in discontinuous phase transitions connected with super-collapse [21, 19] and re-entrant swelling [35]. A deeper understanding of these phenomena, in particular when comparing to experiments, is obtained with a model that resolves the pattern forming instabilities of the gel and the transient dynamics between equilibrium states over a large range of temporal and spatial scales. This will then shed light on the pattern formation processes leading to collapse [26, 42].

The governing equations of such a model are given in a companion paper [4], where we use non-equilibrium thermodynamics to systematically derive a phase-field model of a polyelectrolyte gel. That model accounts for the free energy of the internal interfaces which form upon phase separation, as well as for finite elasticity, together with multi-component transport models via Stefan-Maxwell diffusion. We also derive a thermodynamically consistent model for the ionic bath surrounding the gel. The electro-neutral limit of the full 3D model has been derived via matched asymptotic expansions [14] from which we obtain the jump conditions that need to be imposed at the gel-bath interface. First results from numerical simulations for a 1D constrained gel have been presented in [4], where the possibility of spinodal decomposition – that is, a parameter regime where the uniform equilibrium solution is linearly unstable and hence phase separates in response to infinitesimal perturbations – is raised for the case of a *swelling* gel. Mori et al. [6, 28] also derived and analysed a coupled model for a polyelectrolyte gel in contact with an ionic bath, but do not consider phase separation.

The main goal of this study is to investigate the evolution of collapse via a volume phase transition in a constrained gel by a combination of mathematical techniques. First, we consider the nonlinear equations that determine the homogeneous equilibrium states and deduce the bifurcation that leads to the collapse as the salt concentration in the bath is raised. The numerical solution then reveals the fast initial transients that change the charge distribution in the gel, followed by the appearance of a (solvent) depletion front. This in turn we study via a phase-plane analysis. We systematically investigate the stability of the homogeneous states. This reveals a second route to collapse, where the gel first undergoes spinodal decomposition before the depletion front moves through the heterogeneous state.

The paper is structured as follows. In Section 2 we introduce the electroneutral version of the model for a polyelectrolyte gel, previously derived in [4]. In Section 3 we specialise the model to the case of a one-dimensional constrained gel in contact with an ionic bath, where the thin electric double layer between gel and bath, is replaced by corresponding boundary conditions [14]. In Section 4, we determine the bifurcation diagram for the homogeneous equilibrium states which are controlled by the salt concentration in the bath, and give an overview of various routes to collapse. We carry out numerical simulations that demonstrate the fast dynamics of the free ions that sets the stage for collapse via a moving depletion front. In Section 5 we show the existence of this moving front via a phase plane analysis. Section 6 investigates different parameter regimes that show spinodal decomposition. We use linear stability analysis that identify parameter regimes for spinodal decomposition into localized solvent-rich(poor) phases that eventually coarsen on their path to collapse. In Section

7 we draw our conclusions and give an outlook on further research directions.

2. Governing equations for a polyelectrolyte gel. We consider the problem of a polyelectrolyte gel swelling in a solution (the bath) containing a binary salt. The governing equations are systematically derived in [4], which extends previous models by Drozdov et al. [11] and Hong et al. [17]. In particular, we include the gradient energy to account for the dynamics of collapse and phase separation. As standard in the literature, we consider the electroneutral formulation of the model. In Hennessy et al. [14] we give a detailed derivation of this limit via singular perturbation analysis, where we assume that Debye length and thus the thickness of the double layer at the free interface between the gel and the bath is small compared to the size of the gel.

The governing equation are presented for the full 3D problem in terms of the Eulerian coordinates associated with the current (deformed) configuration. The gel is described as a mixture of three phases: solvent (s), free ions ($+$ and $-$) and the charged polymer network (n). We assume that the fixed charges (with valence z_f) on the polymer network are evenly distributed on the network and account for a fixed fraction $\alpha_f < 1$ of the network volume. In this work we consider z_f to be positive so that the positive ionic species in the solution (with valence z_+) will be denoted as co-ions ($+$) while the negative ones (with valence z_-) will be the counter-ions ($-$). As standard in the polyelectrolyte gel literature, we will assume in what follows that all mobile species (*i.e.*, the solvent and ions) have the same molecular volume ν .

Let us denote by t time and $\mathbf{x} = (x, y, z)$ the Eulerian coordinates, while $\mathbf{X} = \mathbf{X}(\mathbf{x}, t)$ are the corresponding Lagrangian coordinates. Then the gel kinematics are described by the deformation gradient tensor $\mathbf{F} = (\partial \mathbf{X} / \partial \mathbf{x})^{-1}$, with its determinant $J = \det \mathbf{F}$ representing the volume expansion of the gel compared to the dry reference state, where $J = 1$. The velocity of the polymer network \mathbf{v}_n can be expressed as

$$(2.1) \quad \mathbf{v}_n = -\mathbf{F} \frac{\partial \mathbf{X}}{\partial t}.$$

The composition of the gel is described in terms of volume fractions $\phi_i = \phi_i(\mathbf{x}, t)$ with $i \in \{s, +, -, n\}$. Assuming there are no voids in the gel, the volume fractions satisfy

$$(2.2a) \quad 1 = \phi_n + \phi_s + \phi_+ + \phi_-.$$

Moreover, all of the phases are assumed to be incompressible; consequently, J is related to the network volume fraction ϕ_n by $J = \phi_n^{-1}$. The volume fraction occupied by fixed charges is $\phi_f = \alpha_f \phi_n$, where α_f indicates, as defined above, the fraction of volume of the network phase occupied by fixed charges. Since we assume the gel is electrically neutral at each location in space, its net charge must be zero. This introduces the additional constraint

$$(2.2b) \quad z_f \phi_f + z_+ \phi_+ + z_- \phi_- = 0.$$

Conservation of mass and momentum are given by

$$(2.2c) \quad \partial_t \phi_n + \nabla \cdot (\phi_n \mathbf{v}_n) = 0,$$

$$(2.2d) \quad \partial_t \phi_m + \nabla \cdot (\phi_m \mathbf{v}_n) = -\nabla \cdot \mathbf{j}_m,$$

$$(2.2e) \quad \nabla \cdot \mathbf{T} = 0,$$

for $m \in \mathbb{M} = \{s, +, -\}$. Here, \mathbf{T} denotes the Cauchy stress tensor (to be specified below), \mathbf{j}_m are the volumetric fluxes of mobile species relative to the network that

139 moves with velocity \mathbf{v}_n . By differentiating (2.2a) and (2.2b) with respect to time and
 140 using (2.2c)–(2.2d) we obtain

$$141 \quad (2.2f) \quad \nabla \cdot \left(\mathbf{v}_n + \sum_{m \in \mathbb{M}} \mathbf{j}_m \right) = 0,$$

$$142 \quad (2.2g) \quad \nabla \cdot (z_+ \mathbf{j}_+ + z_- \mathbf{j}_-) = 0,$$

144 which are used to replace (2.2c) and (2.2d) for the counter-ions fraction ϕ_- .

145 To complete the model, constitutive relations are required. The fluxes are de-
 146 scribed via Stefan-Maxwell diffusion to account for the relative friction between ions
 147 and solvent,

$$148 \quad (2.3a) \quad \mathbf{j}_s = -\phi_s K \left(\nabla \mu_s + \frac{\phi_+}{\phi_s} \nabla \mu_+ + \frac{\phi_-}{\phi_s} \nabla \mu_- \right),$$

$$149 \quad (2.3b) \quad \mathbf{j}_{\pm} = -\frac{\mathcal{D}_{\pm} \phi_{\pm}}{k_B T} \nabla \mu_{\pm} + \frac{\phi_{\pm}}{\phi_s} \mathbf{j}_s.$$

151 where μ_s , μ_+ and μ_- denote the (electro)chemical potentials of the mobile species,
 152 T is the temperature, k_B is the Boltzmann constant, $K = \mathcal{D}_s/(k_B T)$ is the solvent
 153 permeability and \mathcal{D}_m are the diffusivities of the mobile ions, where we consider $\mathcal{D}_+ =$
 154 $\mathcal{D}_- = \mathcal{D} > \mathcal{D}_s$ in line with the characteristic values reported (see supplementary
 155 material Table SM1 and the literature cited therein [34, 11]). Furthermore, we have
 156 the following expressions for the three chemical potentials

$$157 \quad (2.3c) \quad \mu_s = \mu_s^0 + \nu p - \frac{\gamma}{\nu} \nabla^2 \phi_s + k_B T \left[\ln(\phi_s) + \frac{\chi(1 - \phi_s)}{J} + \frac{1}{J} \right],$$

$$158 \quad (2.3d) \quad \mu_{\pm} = \mu_{\pm}^0 + \nu p + z_{\pm} e \Phi + k_B T \left[\ln(\phi_{\pm}) - \frac{\chi \phi_s}{J} + \frac{1}{J} \right],$$

160 where μ_m^0 are reference chemical potentials, Φ is the electric potential, p is the pres-
 161 sure, e is the elementary charge, χ is the temperature-dependent Flory interaction
 162 parameter and γ is the interfacial stiffness parameter. The latter is associated with
 163 the free energy cost of internal interfaces separating regions of low and high solvent
 164 concentration. The pressure dependence of the ionic chemical potentials (2.3d) is a
 165 result of accounting for the ionic volume fractions in the no-void condition (2.2a) when
 166 deriving the model using an energy-imbalance inequality; see Celora et al. [4] for de-
 167 tails. The pressure dependence of all of the chemical potentials allows stress-assisted
 168 diffusion to be captured in the model. For the stresses in the gel, we consider three
 169 contributions

$$170 \quad (2.3e) \quad \mathbf{T} = -p \mathbf{I} + \mathbf{T}_K + \mathbf{T}_E.$$

172 The first represents an isotropic stress from the fluid pressure with \mathbf{I} denoting the iden-
 173 tity tensor, while \mathbf{T}_K represents the Korteweg stress generated at internal interfaces
 174 (i.e., gradients of the solvent concentration)

$$175 \quad (2.3f) \quad \mathbf{T}_K = \frac{\gamma}{\nu^2} \left[\left(\frac{|\nabla \phi_s|^2}{2} + \phi_s \nabla^2 \phi_s \right) \mathbf{I} - \nabla \phi_s \otimes \nabla \phi_s \right],$$

177 and \mathbf{T}_E is the elastic stress from the response of a neo-Hookean polymer network

$$178 \quad (2.3g) \quad \mathbf{T}_E = \frac{G(\mathbf{B} - \mathbf{I})}{J}.$$

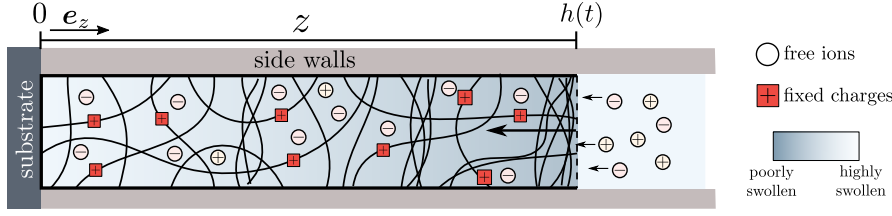


Fig. 1: Schematic of a laterally confined polyelectrolyte gel that collapse along the z -axis only. The free interface with the bath is located at $z = h(t)$. As solvent is expelled by the gel the free interface moves towards the left and salt ions are absorbed/desorbed by the gel so as to maintain electro-neutrality of the gel.

where $\mathbf{B} = \mathbf{F}\mathbf{F}^T$ is the left Cauchy-Green tensor and G is the shear modulus. To close the system, we further need boundary and initial conditions which we derive next for the problem of a constrained gel, which is the focus of this study.

3. Specialisation to constrained swelling and collapse. We consider the case of a constrained gel with monovalent fixed charges ($z_f = +1$) which undergoes uni-axial deformation (in the z direction) due to the uptake or release of a monovalent ($z_{\pm} = \pm 1$) salt solution (see Figure 1). This is analogous to the scenario considered in [9, 15] for the study of constrained swelling and deswelling of neutral hydrogels.

The gel is assumed to be attached to a substrate at $z = 0$ while the interface at $z = h(t)$ is free to move along frictionless side walls that do not influence the bulk behaviour (see [15] for more details). The problem can be reduced to a 1D Cartesian geometry, where the deformation gradient tensor \mathbf{F} and the stress tensor \mathbf{T} have the form

$$(3.1) \quad \mathbf{F} = \text{diag}(1, 1, J(z, t)), \quad \mathbf{T} = \text{diag}(T_\ell(z, t), T_\ell(z, t), T_{zz}(z, t)),$$

and the diffusive fluxes and network velocity are given by $\mathbf{j}_m = j_m(z, t)\mathbf{e}_z$ and $\mathbf{v}_n = v_n(z, t)\mathbf{e}_z$ respectively, with \mathbf{e}_z representing the unit vector in the z direction. Moreover, all variables in (2.2)-(2.3) are assumed to only depend on z and t . At $z = 0$, we assume that the gel is bounded by a solid, insulated, impermeable substrate; hence,

$$(3.2a) \quad v_n(0, t) = 0, \quad j_s(0, t) = 0, \quad j_{\pm}(0, t) = 0.$$

Given the fourth-order derivative in the solvent fraction that ultimately arises from the interfacial term in the solvent chemical potential (2.3c), we need an additional condition on ϕ_s . We assume the solvent is neutral to substrate, resulting in [31]

$$(3.2b) \quad \partial_z \phi_s(0, t) = 0.$$

In most scenarios considered in this paper, we assume that the free surface of the gel at $z = h(t)$ is in contact with an ionic and electro-neutral bath, which behaves like an infinite reservoir of ions. For this scenario, we adapt the boundary conditions derived in [14] starting from the full non-electroneutral model via singular perturbation analysis to account for the formation of a small layer, known as the electric double

layer, near the free interface where electro-neutrality breaks down. Away from the interface with the gel, the volume fraction of ions in the bath is controlled experimentally and set to the value ϕ_0 . In our one-dimensional situation, and assuming the electric potential is zero in the bath, we have

$$(3.3a) \quad T_{zz}(h(t), t) = 0,$$

$$(3.3b) \quad \partial_z \phi_s(h(t), t) = 0,$$

$$(3.3c) \quad \mu_{\pm}(h(t), t) = \mu_{\pm}^0 + k_B T \ln(\phi_0),$$

$$(3.3d) \quad \mu_s(h(t), t) = \mu_s^0 + k_B T \ln(1 - 2\phi_0).$$

To close the system, we further specify a kinematic condition for the boundary $z = h(t)$, which here moves with the gel velocity such that

$$(3.3e) \quad \frac{dh}{dt} = v_n(h(t), t)$$

Having specified the geometry and boundary conditions for the problem, we non-dimensionalise the system as follows:

$$(3.4) \quad \begin{aligned} \hat{\mu}_m &= \frac{\mu_m - \mu_m^0}{k_B T}, \quad \hat{\Phi} = \frac{\Phi e}{k_B T}, \quad \hat{\mathbf{T}} = \frac{\mathbf{T}}{G}, \quad \hat{z} = \frac{z}{L}, \\ \hat{t} &= \frac{t}{\tau}, \quad \hat{p} = \frac{p}{G}, \quad \hat{j}_m = \frac{\nu L}{\mathcal{D}_s} j_m, \quad \tau = \frac{L^2}{\mathcal{D}_s}, \end{aligned}$$

where $m \in \mathbb{M}$ and L is the characteristic size of the gel. The system possesses a second natural length scale, $L_{\text{int}} = \sqrt{\gamma/(\nu k_B T)}$, which characterises the thickness of the internal interfaces that can occur via phase separation of the gel into highly and poorly swollen regions. The ratio of these two length scales gives rise to the non-dimensional parameter $\omega = L_{\text{int}}/L$. Further non-dimensional material parameters are

$$(3.5) \quad \mathcal{G} = \frac{\nu G}{k_B T}, \quad \hat{\mathcal{D}} = \frac{\mathcal{D}}{\mathcal{D}_s}.$$

Note that \mathcal{G} can be related to the number density of polymer chains N_p in the dried network via $\mathcal{G} = N_p \nu$, which helps in the estimation of its value (see Table SM1). We introduce the scalings into the 1D model and then drop the hat notation, so that the non-dimensional governing equations read

$$(3.6a) \quad \partial_t \phi_s + \partial_z(\phi_s v_n) = -\partial_z j_s,$$

$$(3.6b) \quad \partial_t \phi_+ + \partial_z(\phi_+ v_n) = -\partial_z j_+,$$

$$(3.6c) \quad \partial_z T_{zz} = 0,$$

From (2.2f)-(2.2g), we obtain $\partial_z(v_n + j_s + j_+ + j_-) = 0$ and $\partial_z(j_+ - j_-) = 0$ which we can integrate imposing the no-flux condition at $z = 0$ to get:

$$(3.6d) \quad j_+ = j_-,$$

$$(3.6e) \quad v_n = -j_s - 2j_+.$$

We can use (3.6d) to eliminate the electric potential Φ from the model, which can be obtained by solving

$$(3.7a) \quad \partial_z \Phi = \partial_z (\mathcal{G} p + \ln \phi_- - \chi \phi_s \phi_n + \phi_n) + \frac{j_+}{\phi_- \mathcal{D}} - \frac{j_s}{\phi_s \mathcal{D}}.$$

The Dirichlet boundary condition for Eq. (3.7a) is derived by subtracting Eqs. (3.3c) and using the definition of the chemical potentials μ_{\pm} (see Eqs. (2.3d)) and is given by:

$$(3.7b) \quad \Phi(h(t), t) = \frac{1}{2} \ln \left(\frac{\phi_-}{\phi_+} \right) \Big|_{z=h(t)}.$$

Similarly we eliminate the pressure from the model by integrating $\partial_z(T_{zz}) = 0$ and applying the boundary condition (3.3a), which leads to

$$(3.8) \quad p = \frac{\omega^2}{\mathcal{G}} \left[\phi_s \partial_{zz} \phi_s - \frac{(\partial_z \phi_s)^2}{2} \right] + \frac{(1 - \phi_n^2)}{\phi_n},$$

The evolution of the gel composition is therefore dictated by the following two governing equations:

$$(3.9a) \quad \partial_t \phi_s + \partial_z(\phi_s v_n) = -\partial_z j_s,$$

$$(3.9b) \quad \partial_t \phi_+ + \partial_z(\phi_+ v_n) = -\partial_z j_+.$$

which is coupled to the constitutive laws (2.3)

$$(3.10a) \quad j_s = -\frac{\phi_s^2}{1 - \phi_n} \partial_z \mu_s + \frac{2\phi_s}{(1 - \phi_n)\mathcal{D}} j_+,$$

$$(3.10b) \quad j_+ = -\frac{\mathcal{D}\phi_+\phi_-}{\phi_+ + \phi_-} \partial_z \bar{\mu} + \frac{2\phi_+\phi_-}{\phi_s(\phi_+ + \phi_-)} j_s,$$

$$(3.10c) \quad v_n = -j_s - 2j_+,$$

$$(3.10d) \quad \bar{\mu} = A(\phi_s, \phi_+) + 2\omega^2 \phi_s \partial_{zz} \phi_s - \omega^2 (\partial_z \phi_s)^2,$$

$$(3.10e) \quad \mu_s = B(\phi_s, \phi_+) - (1 - \phi_s) \omega^2 \partial_{zz} \phi_s - \frac{\omega^2}{2} (\partial_z \phi_s)^2,$$

$$(3.10f) \quad \phi_n = \frac{1 - \phi_s - 2\phi_+}{1 + \alpha_f},$$

$$(3.10g) \quad \phi_- = \frac{\phi_+ + (1 - \phi_s - \phi_+)\alpha_f}{1 + \alpha_f}.$$

In Eq. (3.10b), $\bar{\mu}$ is defined as the dimensionless chemical potential of the free ions ($\bar{\mu} = \mu_+ + \mu_-$) and (3.10d) is obtained by summing over (2.3d) after non-dimensionalisation according to the scaling given in (3.4). The functions A , B are defined as follows:

$$(3.10h) \quad A(\phi_s, \phi_+) = \ln \left(\phi_+ \frac{\phi_+ + (1 - \phi_s - \phi_+)\alpha_f}{1 + \alpha_f} \right) + 2[1 - \chi\phi_s] \frac{1 - \phi_s - 2\phi_+}{1 + \alpha_f} + \frac{2\mathcal{G}}{1 + \alpha_f} \frac{(1 + \alpha_f)^2 - (1 - \phi_s - 2\phi_+)^2}{1 - \phi_s - 2\phi_+},$$

$$(3.10i) \quad B(\phi_s, \phi_+) = \ln \phi_s + [\chi(1 - \phi_s) + 1] \frac{1 - \phi_s - 2\phi_+}{1 + \alpha_f} + \frac{\mathcal{G}}{1 + \alpha_f} \frac{(1 + \alpha_f)^2 - (1 - \phi_s - 2\phi_+)^2}{1 - \phi_s - 2\phi_+}.$$

The system is closed by imposing the boundary conditions:

$$(3.11a) \quad \partial_z \phi_s(h(t), t) = 0,$$

$$(3.11b) \quad \mu_s(h(t), t) = \ln(1 - 2\phi_0),$$

$$(3.11c) \quad \bar{\mu}(h(t), t) = 2 \ln(\phi_0).$$

Here (3.11a)-(3.11b) are the dimensionless counterpart of (3.3b)-(3.3d), while (3.11c) is obtained by summing over the dimensionless form of (3.3c). In one case, Fig. 12 (and in Fig. SM1 in the supplemental materials), we also consider the scenario in which the gel is isolated from the bath. When this is the case, the boundary conditions (3.11b)-(3.11c) are replaced by no-flux conditions at the free interface (since mobile species are trapped in the gel). Moreover, (3.7b) is replaced with a grounding condition at $z = h(t)$. Hence, for an isolated bath we impose

$$(3.12a) \quad \partial_z \phi_s(h(t), t) = 0,$$

$$(3.12b) \quad j_s(h(t), t) = j_+(h(t), t) = 0,$$

$$(3.12c) \quad \Phi(h(t), t) = 0.$$

Unless otherwise stated, the parameters used in the simulations are

$$(3.13a) \quad \alpha_f = 0.04, \mathcal{D} = 5, \chi = 0.78, \mathcal{G} = 2 \times 10^{-4}, \omega = 0.025.$$

We further consider the the volume fraction of ions in the bath, ϕ_0 , to change at time $t = 0$ from $\phi_{0-} = 10^{-6}$ to a new value ϕ_{0+} . For the latter we consider two scenarios:

$$(3.13b) \quad \text{set 1: } \phi_{0+} = 10^{-4} \quad \text{and} \quad \text{set 2: } \phi_{0+} = 10^{-2}.$$

The details on the numerical methods used to solve the system (3.9)-(3.10) in the different scenarios can be found in the supplemental material Section SM2. We note that the rescaled spatial variable which maps the gel to a fixed domain is denoted by $Z = z/h(t) \in [0, 1]$.

4. Homogeneous equilibrium states and routes to collapse. We now consider the system (3.9)-(3.10) for ϕ_s and ϕ_+ in equilibrium with an ionic bath. More specifically, we consider homogeneous, flux-free steady states that satisfy the boundary conditions (3.2)-(3.3). The equilibrium states are denoted by (ϕ_s^*, ϕ_+^*) and satisfy

$$(4.1a) \quad A(\phi_s^*, \phi_+^*) - 2 \ln(\phi_0) = 0,$$

$$(4.1b) \quad B(\phi_s^*, \phi_+^*) - \ln(1 - 2\phi_0) = 0.$$

Recall that ϕ_0 denotes the volume fraction of ions in the surrounding bath. The conditions (4.1) define the generalisation of the Donnan equilibrium [10] as it applies to our situation, i.e. a polyelectrolyte gel with its fixed charges and the mobile species represented by the salt ions [20].

Considering the shear modulus of the gel \mathcal{G} to be fixed, we investigate how the equilibria depend on the concentration of ions in the bath ϕ_0 and the Flory interaction parameter χ . For large shear moduli \mathcal{G} , as in Fig. 2b, there is a unique homogeneous equilibrium solution. Although variations of ϕ_s^* along ϕ_0 are small, there is a sensitive dependence on the Flory interaction parameter χ .

For small \mathcal{G} , as in Fig. 2a, there is a range of χ for which the system either exhibits one or three equilibrium states, depending on the value of the salt fraction in the bath

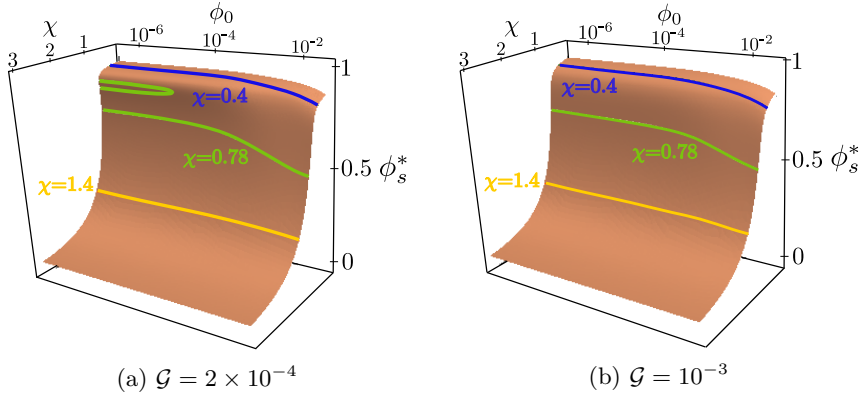


Fig. 2: Surfaces of homogeneous equilibrium solutions for the volume fraction of solvent in the gel ϕ_s^* . The equilibrium solutions are obtained by solving (4.1) using the parameter values in (3.13a). The surfaces are plotted in terms of the salt fraction in the bath ϕ_0 and the Flory parameter χ . The solid lines represent level sets at fixed values of χ .

ϕ_0 . A value of $\chi = 0.78$ lies within this range, for example. For large values of ϕ_0 , a single equilibrium solution exists that is characterised by a small concentration of solvent, i.e. the equilibrium corresponds to a collapsed state. As ϕ_0 is decreased, a disconnected branch of equilibrium solutions appears. This new branch consists of two highly swollen equilibrium states. The stability of these three equilibria will be characterized in Section 6. In summary, the collapsed and most-swollen equilibrium states are stable, whereas the state with an intermediate degree of swelling is unstable. A volume phase transition will occur when the gel is driven off the stable swollen branch onto the stable collapsed branch by an increase in ϕ_0 .

4.1. Routes to collapse. Our aim is to understand the dynamic response of the gel during the volume phase transition. The analysis in subsequent sections will reveal that the volume phase transition can follow one of two routes, which we summarise in the panels in Fig. 3. For the parameter values in (3.13a), the equilibrium solvent fraction is plotted as a function of the salt fraction in the bath ϕ_0 in Fig. 3 (a). The red square on the swollen branch when $\phi_0 = 10^{-6}$ denotes the initial state of the gel that we consider here.

An example of the first route to the gel collapse occurs when ϕ_0 is increased to 10^{-4} , which we call set 1 in (3.13). In this case, a deswelling front propagates into the gel from the free surface. A snapshot of a numerical simulation, which depicts the propagating front by plotting the solvent fraction as a function of space, is provided in Fig. 3 (b). Simulation details can be found in Sec. 5. The deswelling front separates two homogeneous states that are not equilibrium solutions. The properties of the front can be predicted from a phase-plane analysis of the steady model (5.3), which will be presented in Sec. 5.1. By exploiting the diluteness of the ions, the steady model (5.3) reduces to a pair of first-order differential equations for the solvent fraction ϕ_s and its gradient $\partial_z \phi_s$ given by (5.9). The deswelling front is well approximated by a heteroclinic orbit that exists in the phase plane of (5.9), shown schematically in Fig. 3 (c).

An example of the second route to gel collapse occurs when ϕ_0 is increased to

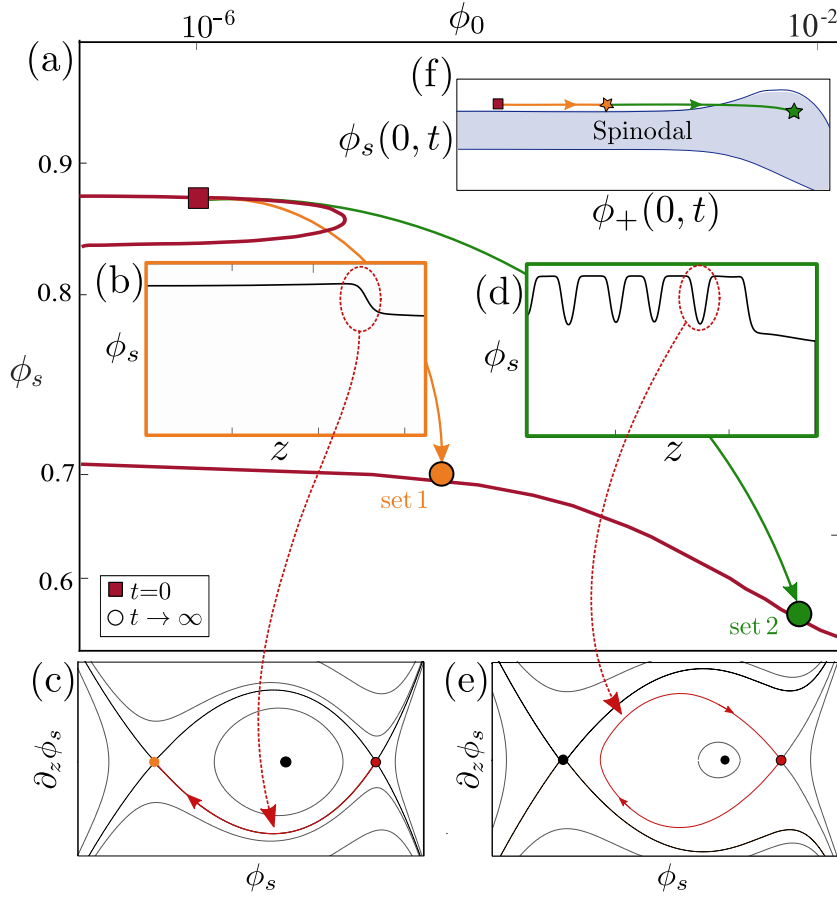


Fig. 3: Summary of the two routes to collapse. (a) Equilibrium solvent fraction obtained by solving (4.1) using the parameter values in (3.13a). A volume phase transition is triggered by increasing the salt fraction in the bath ϕ_0 from 10^{-6} (red square) to 10^{-4} (set 1; orange circle) or 10^{-2} (set 2; green circle). (b) Set 1 leads to the first route to collapse, where a deswelling front invades the gel from the free surface, which is seen by plotting the solvent fraction as a function of space; simulation details can be found in Sec. 5. (c) A heteroclinic orbit of (5.9), which provides an approximation to the propagating front; see Sec. 5.1. (d) The second route to collapse involves front propagation and spinodal decomposition in the bulk of the gel. Simulation details are provided in Sec. 6.2. (e) A two-dimensional projection of a homoclinic orbit of (5.9); these orbits provide approximations of the phases that form within the bulk of the gel during the second route to collapse; see Sec. 6.2. (f) Evolution of the solvent and cation fraction at the substrate ($z = 0$) for parameter set 1 (orange) and set 2 (green). Stars denote the composition after the front has formed. The linearly unstable spinodal regime is shaded and computed in Sec. 6.1. For more information about the panels, see Sec. 4.1. All panels except (a) are to be interpreted schematically.

10^{-2} , which we call set 2 in (3.13). In this case, front propagation occurs, but the bulk of the gel undergoes spinodal decomposition, leading to isolated, solvent-poor phases spontaneously appearing. A snapshot of a numerical simulation (see Sec. 6.2) is provided in Fig. 3 (d), which shows the solvent fraction as a function of space and the emergence of collapsed phases in the bulk. In Sec. 6.2, we show that the solvent-poor phases are well approximated by homoclinic orbits that exist in the phase space for (5.3). Two-dimensional projections of these orbits are shown schematically in Fig. 3 (e).

A linear stability analysis of the full time-dependent model, carried out in Sec. 6.1, elucidates why the volume phase transition has two routes. The first route to collapse occurs when the bulk of the gel has a composition that is linearly stable. That is, the bulk composition remains outside of the linearly unstable region of the phase diagram (this region is called the spinodal region). This is illustrated in Fig. 3 (f), which tracks how the solvent and cation fraction at the substrate ($z = 0$) evolve during the volume phase transition. The orange star represents the composition after front propagation is initiated. The path that is traced out in the phase diagram avoids the spinodal (shaded) region. The second route to collapse occurs when the bulk of the gel has a composition that is linearly unstable. In this case, the formation of a propagating front pushes the bulk composition into the spinodal region, as shown by the path to the green star in Fig. 3 (f).

5. Front propagation in a collapsing gel. We start by investigating the simpler scenario of collapse driven uniquely by propagation of a depletion front using numerical simulations of Eqs. (3.9)-(3.11) with parameter values given by set 1 in Eqs. (3.13). Results from the numerics are used to generate Figs. 4-5. We find that the collapse of the gel is characterised by two time-scales: the first is dictated by the fast diffusion of ions into the gel that precede the onset of the depletion front, while the second by the slower transport of solvent into the gel. The presence of these two time-scales is evident in Fig. 4a where we illustrate the trajectory the volume fraction ϕ_s and ϕ_+ in the bulk of the gel; specifically, at the substrate ($Z = 0$) in the (ϕ_+, ϕ_s) -plane. As shown in Fig. 4a, for $t \sim O(10^2)$, the ion concentration in the interior of the gel quickly increases while ϕ_s remains approximately constant. As the gel is initially highly swollen, i.e. $\phi_+ \ll \phi_s$, the gel size is determined by the concentration of solvent, and so remains approximately constant during this first transient (see Fig. 4c), i.e. $h(t) \approx h(0)$ for $t \sim O(10^2)$ with $h(0) \approx (1 - \phi_s(0))^{-1} \approx 8$. Focusing on the evolution of ϕ_+ (see Fig. 4b), we see that within less than one time unit, the concentration builds up at the boundary and subsequently penetrates into the gel. At $t = 12$, the process has almost concluded and in fact, early signs of a new front manifest themselves at the free interface, which becomes more pronounced at $t = 301$. Together with the ion concentration, the generalised chemical potential $\bar{\mu}$ move from its initial value $2 \ln(\phi_{0-})$ to approximately $2 \ln(\phi_{0+})$. This difference in chemical potential drives the process of ion diffusion. Since the flux of ions is \mathcal{D} times the gradient of the chemical potential (and the domain size $h(0) \approx 8$), we can estimate the time scale of ionic diffusion as $t \sim [h(0)]^2 / [2\mathcal{D} \ln(\phi_{0+}/\phi_{0-})] \approx 2.15$, which is consistent with the observation in the numerical simulations. Using a scaling argument we can also estimate the concentration of ions in the gel prior and after the transient. Given that the concentration of ions in the bath is small, i.e. $\phi_0 \ll 1$, the logarithmic term $\ln \phi_0$ in (4.1a) becomes large and needs to be balanced. Since the gel is not too swollen, i.e. $1 - \phi_s - 2\phi_+ \gg \phi_0$, or dry, i.e. $\phi_n^{-1}\mathcal{G} \ll 1$ the only term in

(3.10h) that can balance $\ln \phi_0$ is the logarithmic term so that

$$(5.1) \quad \phi_+ \frac{\phi_+ + \alpha_f(1 - \phi_s - \phi_+)}{1 + \alpha_f} \sim \phi_{0+}^2.$$

and given the chosen value of α_f (see 3.13)), the balance (5.1) gives

$$(5.2) \quad \phi_+ \sim \phi_{0+}^2(1 - \phi_s)^{-1}/\alpha_f,$$

so that we predict the concentration of ions to be $\phi_+ \sim 1.25 \times 10^{-10}$ prior to $t = 0$ and $\phi_+ \sim 1.25 \times 10^{-6}$ after the fast ion diffusion (given $(1 - \phi_s)^{-1} \approx 8$). These are in good agreement with numerical result in Fig. 4b. After the ion concentration has

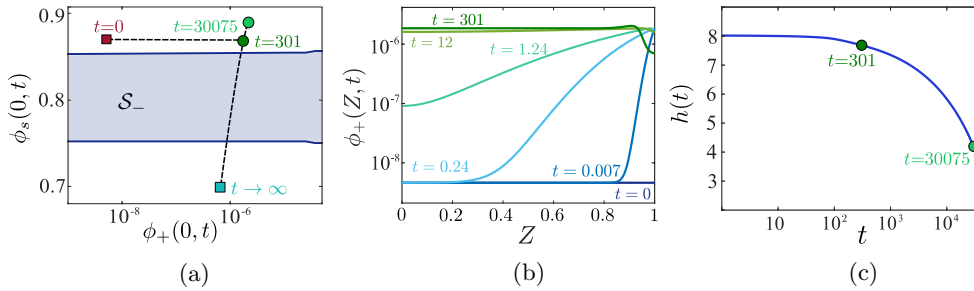


Fig. 4: Numerical solutions of Eqs. (3.9)-(3.11) for the case of a dilute bath for the parameter set 1 in (3.13). (a) Evolution of the solution at the substrate (i.e. $Z = 0$) in the (ϕ_s, ϕ_+) plane. The instability region \mathcal{S}_- , defined by Eq. (6.6) (see stability analysis in Section 6) is highlighted in blue. (b) Evolution of the ion fraction $\phi_+(Z, t)$. (c) Time evolution of the size of the gel (colour of the dots corresponds to those points used in panel (a)).

equilibrated, a slower process takes place, whereby solvent is removed from the gel through the aforementioned depletion front. This is illustrated in Fig. 5, where we present snapshots in time of the gel composition (see first row). For the same time points of the snapshots we also illustrate the values of the volume fractions, fluxes and electric field in the gel. The front is clearly seen in the concentration profiles for the solvent ϕ_s as well as for the mobile ion species ϕ_+ and the gradient of the electric potential $-\partial_z \Phi$, i.e. the electric field in the gel. In the poorly swollen region of the gel (near the free interface), $\phi_s \approx 0.7$; using the scaling (5.2) we therefore expect a reduction in the concentration of ions, more precisely we obtain $\phi_+ \sim 8 \times 10^{-7}$ which is again in line with the numerical results. In the last column ($t = 42500$), the front has reached the substrate and the gel has collapsed with its composition having reached a new state (see ‘powder’ blue square in Fig. 4a). The solvent flux j_s is only on the order of 10^{-4} , hence the appropriate time scale for the depletion front movement is $O(10^4)$. The main contribution is from the gradient of the chemical potential μ_s which is set by the function B (see Eq. (3.10i)). The latter is connected with \mathcal{G} , which is small and it is this small value that determines the slow collapse.

To summarize (as illustrated in Fig. 4a), the gel starts from a state of high concentration of solvent and a small concentration of co-ions. From there, it quickly evolves to a new state with higher salt content. As derived in Section 6 and shown in Fig. 4a, both of these states are stable and show no sign of spinodal decomposition. Instead,

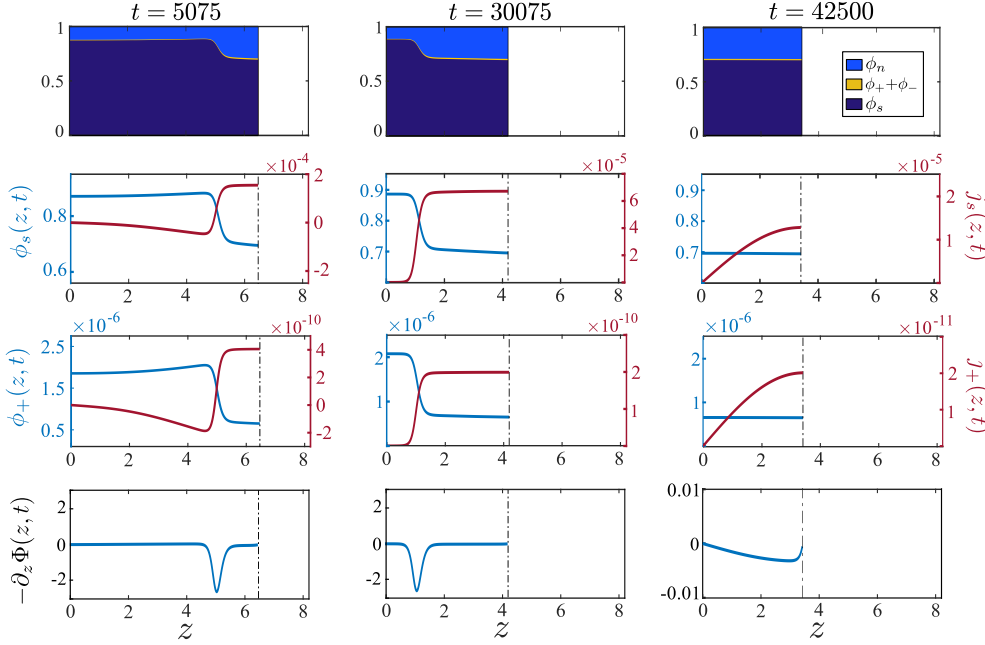


Fig. 5: Numerical solution of the model (3.9)-(3.10) for parameter set 1 in (3.13) and boundary conditions (3.11) (same scenario as Fig. 4): The first row illustrates the gel composition at different points in time. For the same time points we also plot the volume fractions, the corresponding fluxes and the electric field $-\partial_z \Phi$ (defined by using (3.7a)).

a depletion front moves through the gel. At later time (i.e. $t \sim 30000$), as the front approaches the substrate, the solvent concentration $\phi_s(0, t)$ increases slightly before decreasing to its new linearly stable steady state value, with a slightly higher salt but a much lower solvent concentration.

5.1. Phase-plane analysis. The slow movement of the depletion fronts on the diffusive time scale suggests that these structures are in a quasi-stationary state, which simplifies their analysis by enabling the time derivatives and fluxes from the system (3.9)-(3.10) to be neglected, so that the solution will only depend on the spatial variable z . Since fluxes are negligible, μ_s , $\bar{\mu}$ are almost constant (independent of z) in an $O(1)$ vicinity of the front. With this assumption and after rescaling z with ω , we have,

$$(5.3a) \quad \partial_z \phi_s = q$$

$$(5.3b) \quad \partial_z q = \frac{1}{1 - \phi_s} [B(\phi_s, \phi_+) - \mu_s] - \frac{1}{2(1 - \phi_s)} q^2$$

$$(5.3c) \quad \mu_s = \frac{\phi_s - 1}{2\phi_s} [\bar{\mu} - A(\phi_s, \phi_+)] + B(\phi_s, \phi_+) - \frac{1}{2\phi_s} q^2,$$

where A and B are as defined by (3.10h)-(3.10i), and we introduce the auxiliary variable q . The fixed points $(q, \phi_s, \phi_+) = (0, \phi_s^0, \phi_+^0)$ of the system (which correspond

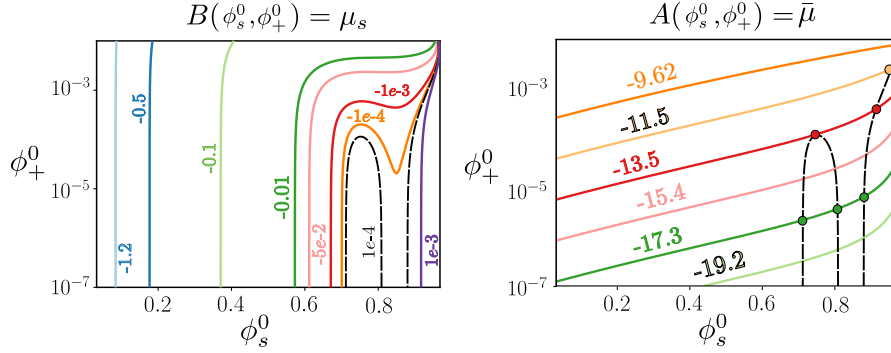


Fig. 6: Level sets for the functions A and B (defined by Eqs. (3.10h)-(3.10i)) that define the fixed points of the system (5.3), note that the functions are expressed in terms of ϕ_s^0 and ϕ_+^0 . The dashed line in right panel is taken from the left one (i.e. $\mu_s \equiv 10^{-4}$). The value of the parameters χ , α_f and \mathcal{G} are given in Eq. (3.13a).

to homogeneous equilibrium states for the full model) are found from (5.3) via

$$(5.4) \quad A(\phi_s^0, \phi_+^0) = \bar{\mu}, \quad B(\phi_s^0, \phi_+^0) = \mu_s.$$

As shown in Fig. 6 the number of fixed points varies depending on the values assigned to μ_s and $\bar{\mu}$. For sufficiently small values of μ_s (see $\mu_s = -0.1$ for example) the system has a unique fixed point. As we increase the value of μ_s there is an intermediate region near $\mu_s = 0$ where multiple fixed points can exist depending on the values of $\bar{\mu}$. As shown on the right-hand side panel of Fig. 6, when considering $\mu_s = 10^{-4}$, the system has three fixed points when $\bar{\mu}$ is below a critical negative value, i.e. in the dilute limit $\phi_+^0 \ll 1$. As $\bar{\mu}$ increases, the system undergoes a saddle-node bifurcation resulting in a unique fixed point. Note that the equilibrium states computed in Section 4 are a subset of the fixed points of the system (5.3) as the value of μ_s and $\bar{\mu}$ are not independent as they are set by the ionic bath via the boundary conditions (3.11b)-(3.11c). For our local analysis we note that the depletion front represents a narrow, slowly moving transition between two almost homogeneous states, so that we can approximate it by a quasi-stationary solution that tends to homogeneous states as $z \rightarrow \pm\infty$. We then linearise around $(0, \phi_s^0, \phi_+^0)$ and determine the number of modes consistent with these limits, which we then use to carry out a degree of freedom count. We make the ansatz

$$(5.5) \quad \phi_s = \phi_s^0 + \delta \phi_s^1 e^{sz}, \quad q = \delta q^1 e^{sz}, \quad \phi_+ = \phi_+^0 + \delta \phi_+^1 e^{sz},$$

with $\delta \ll 1$, and s being a constant. Inserting this, we obtain at $O(\delta)$ the condition

$$(5.6) \quad \begin{bmatrix} B_{\phi_s} - (1 - \phi_s^0)s^2 & B_{\phi_+} \\ (1 - \phi_s^0)A_{\phi_s} + 2\phi_s^0 B_{\phi_s} & (1 - \phi_s^0)A_{\phi_+} + 2\phi_s^0 B_{\phi_+} \end{bmatrix} \begin{bmatrix} \phi_s^0 \\ \phi_+^0 \end{bmatrix} = 0,$$

where the subscripts ϕ_s and ϕ_+ denote partial derivatives of A and B , which are evaluated at the equilibrium point (ϕ_s^0, ϕ_+^0) . In order for the system to have non-trivial solutions, we must set the determinant of the coefficient matrix to zero, which

471 gives

$$472 \quad (5.7) \quad s^2 = \frac{A_{\phi_+} B_{\phi_s} - A_{\phi_s} B_{\phi_+}}{(1 - \phi_s^0) A_{\phi_+} + 2\phi_s^0 B_{\phi_+}}.$$

473 We therefore conclude that the equilibrium is a saddle point if $s^2 > 0$. We now seek a
 474 non-homogeneous quasi-stationary solution connecting two saddle points, $(0, \phi_s^a, \phi_+^a)$
 475 and $(0, \phi_s^b, \phi_+^b)$. This corresponds to imposing the far-field conditions $(\phi_s, \phi_+) \rightarrow$
 476 (ϕ_s^a, ϕ_+^a) and $(\phi_s, \phi_+) \rightarrow (\phi_s^b, \phi_+^b)$ as $z \rightarrow -\infty$ and $z \rightarrow +\infty$, respectively. When
 477 considering the degrees of freedom in the solution, we have one mode for each saddle
 478 point which is consistent with the limit, namely $s^a < 0$ for $(0, \phi_s^a, \phi_+^a)$ and $s^b > 0$ for
 479 $(0, \phi_s^b, \phi_+^b)$. These account for two degrees of freedom, which, together with the two
 480 unknown constants μ_s and $\bar{\mu}$, add up to four degrees of freedom. The system (5.3)
 481 is second order and hence removes two degrees of freedom, and the invariance of any
 482 solution with respect to translations along the z -axis subtracts another one. Hence
 483 one degree of freedom remains, and this is associated with $\bar{\mu}$, which needs to be given.
 484 We note that a full expansion at higher orders about the quasi-stationary solution
 485 might lead to additional constraints that fixes the degree of freedom remaining in
 486 the system. However, this goes beyond the purpose of this analysis, which aims at
 487 understanding the structure of the depletion front.

488 **5.1.1. The limit of dilute salt concentrations.** We here consider the limit of
 489 dilute salt concentration, i.e. $\phi_+ \ll \phi_s < 1$, which is representative of the numerical
 490 results from Fig. 5. Here, we use the same equations and boundary conditions and
 491 the same parameter set, where ϕ_+ is small. Inspired by the scaling (5.2), we rescale
 492 the model variables, via

$$493 \quad (5.8) \quad \phi_+ = \alpha_f \epsilon^2 \tilde{\phi}_+, \quad \bar{\mu} = 2 \ln(\alpha_f \epsilon) + \tilde{\mu}.$$

494 where the dilute limit is therefore taken by considering $\epsilon \rightarrow 0$. Note that if we define
 495 $\epsilon = \phi_{0+}/\alpha_f$, we recover (5.2) up to a factor $1 - \phi_s$ allowing us to relate the phase
 496 plane analysis to the numerical simulations in the presence of a bath (which is instead
 497 here neglected). Substituting (5.8) into (5.3) and considering only the leading order
 498 problem in this limit, we obtain

$$499 \quad (5.9a) \quad \partial_z \phi_s = q$$

$$500 \quad (5.9b) \quad \partial_z q = \frac{1}{1 - \phi_s} [B_0(\phi_s) - \mu_s] - \frac{1}{2(1 - \phi_s)} q^2$$

$$501 \quad (5.9c) \quad \mu_s = \frac{1 - \phi_s}{2\phi_s} [A_0(\phi_s, \tilde{\phi}_+) - \tilde{\mu}] + B_0(\phi_s) - \frac{1}{2\phi_s} q^2,$$

503 with

$$504 \quad (5.9d) \quad A_0(\phi_s, \tilde{\phi}_+) = \ln \left[\left(\frac{1 - \phi_s}{1 + \alpha_f} \right) \frac{\tilde{\phi}_+}{\phi_s^2} \right] - 2\chi \left(\frac{1 - \phi_s}{1 + \alpha_f} \right) + 2B_0(\phi_s),$$

$$505 \quad (5.9e) \quad B_0(\phi_s) = \ln(\phi_s) + (\chi(1 - \phi_s) + 1) \left(\frac{1 - \phi_s}{1 + \alpha_f} \right) + \mathcal{G} \frac{(1 + \alpha_f)^2 - (1 - \phi_s)^2}{(1 + \alpha_f)(1 - \phi_s)}.$$

507 Equations (5.9a) and (5.9b) decouple from the algebraic constraint (5.9c). The first
 508 integral of (5.9a) and (5.9b) is then used to investigate the phase plane as a function

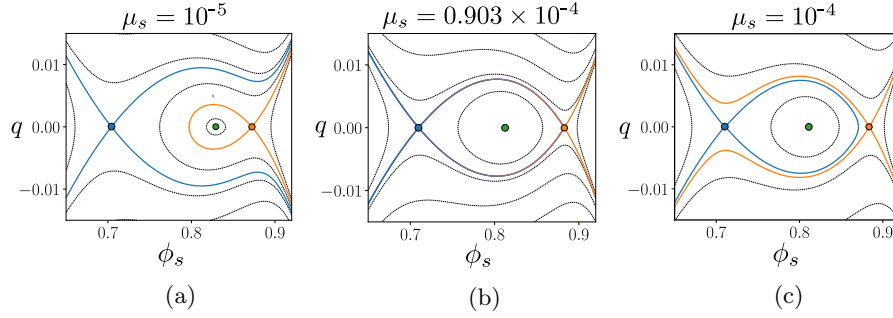


Fig. 7: Phase plane analysis for the dilute limit (*i.e.*, Eqs. (5.9a) and (5.9b)) with parameters as in (3.13a) and three different value of μ_s : (a) $\mu_s < \mu_s^{(c)}$; (b) $\mu_s = \mu_s^{(c)}$ for which there is an heteroclinic orbit connecting the two equilibrium state; (c) $\mu_s > \mu_s^{(c)}$. Fixed point are highlighted by small circles, trajectories leaving from or asymptoting into fixed points are indicated by solid coloured line, while all other trajectories are denoted by dashed black line.

of the chemical potential μ_s as illustrated in Fig. 7. In contrast to a non-ionic hydrogel [15], the contribution of the fixed charges allows multiple fixed points to exist when $\mu_s = 0$, *i.e.* for a gel in contact with pure water. There is a unique critical value of μ_s , denoted by μ_s^c , for which the two saddle points are connected by an heteroclinic orbit, corresponding to a front-type non-homogeneous quasi-stationary solution (see Fig. 7b). If $\mu_s < \mu_s^c$ as shown in Fig. 7a, there is a homoclinic orbit attached to the right fixed point (*i.e.* the orange point), corresponding to a quasi-stationary solution with a localised solvent-depleted zone. On the contrary, for $\mu_s > \mu_s^c$, the homoclinic orbit is attached to the left fixed point (*i.e.* the blue point; see Fig. 7c), which represents a localised solvent-rich zone. We can find the critical value of μ_s by combining (5.9a) and (5.9b) into a second-order equation and using $f = 1/\sqrt{1-\phi_s}$ as an integrating factor to obtain

$$(5.10a) \quad \int_{\phi_s^a}^{\phi_s^b} \frac{B_0(\phi_s) - \mu_s}{(1-\phi_s)^2} d\phi = 0,$$

$$(5.10b) \quad B_0(\phi_s^a) - \mu_s = 0, \quad B_0(\phi_s^b) - \mu_s = 0,$$

where ϕ_s^a and ϕ_s^b are the values of the solvent fraction at the two saddle points. Note that this is a Maxwell condition for the co-existing states ϕ_s^a and ϕ_s^b , which are independent of the ion fraction $\tilde{\phi}_+$ in the dilute limit. Solving numerically the system with the parameters for α and χ and \mathcal{G} corresponding parameter set 1 in (3.13) gives

$$(5.11) \quad \mu_s = 0.903 \times 10^{-4}, \quad \phi_s^a = 0.883, \quad \phi_s^b = 0.710.$$

As shown in Fig. 8, the phase plane analysis is overall in good agreement with the dynamical simulation from Fig. 5. While the value of μ_s at the free interface (*i.e.* $Z = 1$) is set by the bath, in the bulk of the gel μ_s sets around the critical value obtained by our phase-plane analysis (see Eq. (5.11)). Note that provided $\tilde{\mu}$ is known from the numerical simulations, we can use the constraint (5.9c) to compute $\tilde{\phi}_+$. In this set of simulations, we find $\tilde{\mu} \in (2.75 \times 10^{-8}, 3.89 \times 10^{-4})$, that is, $\tilde{\mu} \ll \ln(\epsilon\alpha_f)$, and therefore, see (5.8), we have set it to zero for the phase plane solutions involving parameter set 1.

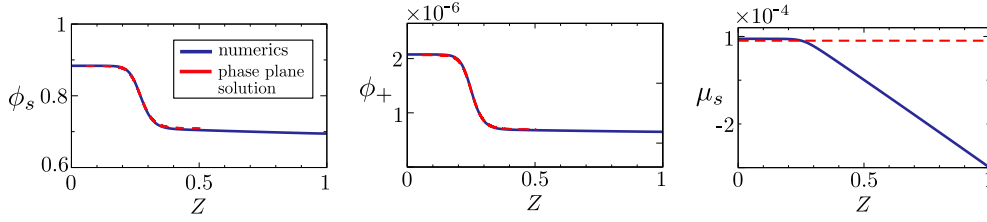


Fig. 8: Comparison of the asymptotic approximation for the phase-plane solution (5.9)–(5.10) (shown with dashed red lines) for ϕ_s , ϕ_+ and μ_s with the numerical results from Fig. 5 at a time $t = 30075$ when the concentration profile fronts have settled into a quasistationary state (solid black lines), using the parameter set 1 in (3.13). A single shift along the Z -axis was applied to all phase plane profiles so that ϕ_s matches the numerical solution at $\phi_s = 0.8$.

5.1.2. The general case. We now explore the non-dilute limit. This requires solving the general case of (5.3)–(5.4) which is done numerically applying a shooting method. Starting from slightly perturbed values for the left state, we integrate the resulting initial value problem for a system of differential algebraic equations (DAEs), rewritten in terms of ϕ_s and ϕ_+ as the dependent variables. For a fixed the value of $\tilde{\mu}$, there is a unique value of μ_s such that the trajectory connects to the right equilibrium. The critical value of μ_s is then determined using a bisection iteration. The resulting solution defines μ_s and the associated values for the left and right state ϕ_s^a and ϕ_s^b for ϕ_s and similarly for ϕ_- . For the case of $\tilde{\mu}$ equal to zero, the results are shown

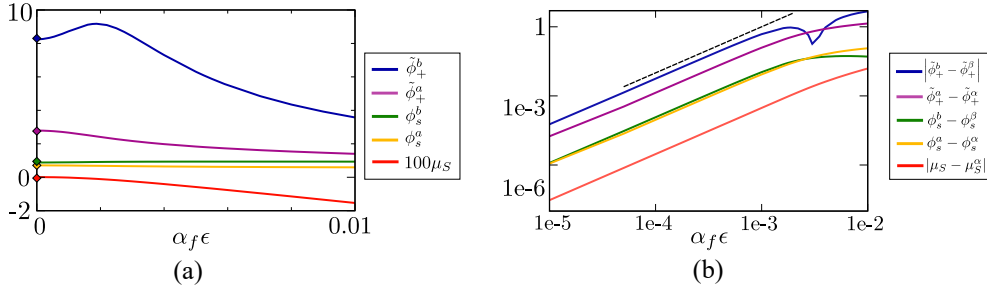


Fig. 9: (a) The figure shows graphs of $100\mu_s$, ϕ_s^a , ϕ_s^b , $\tilde{\phi}_+^a$ and $\tilde{\phi}_+^b$, listed in order from bottom to top. The diamonds at $\epsilon = 0$ represent the values $100\mu_s^\alpha$, ϕ_s^α , ϕ_s^β , $\tilde{\phi}_+^\alpha$ and $\tilde{\phi}_+^\beta$ obtained from the asymptotic solution as given by (5.11) and (5.9c). (b) This log-log plot has graphs for $|\mu_s - \mu_s^\alpha|$, $\phi_s^a - \phi_s^\alpha$, $\phi_s^b - \phi_s^\beta$, $\tilde{\phi}_+^a - \tilde{\phi}_+^\alpha$, $|\tilde{\phi}_+^b - \tilde{\phi}_+^\beta|$. The short top line represents a quadratic function, and is included to guide the eye.

in Fig. 9. The plots in (a) show graphs of the values for $100\mu_s$ and for the values of the two equilibrium states for ϕ_s^0 and $\tilde{\phi}_+^0$ as a function of $\phi_{0+} = \alpha_f \epsilon$. solution (5.10). Moreover, near to $\epsilon = 0$, the behaviour is quadratic, as can be seen from the log-log plot in Fig. 9 (b), consistent with neglecting $O(\epsilon^2)$ -terms in (5.9). However, for $\alpha_f \epsilon$ greater than 1×10^{-3} , the value for $\tilde{\phi}_{+,2}$ departs from this behaviour and in fact passes through a maximum as it reverses its trend. We remark that μ_s is positive for $\alpha_f \epsilon \leq 5.45 \times 10^{-3}$, and negative for larger values of ϵ .

A comparison between DAE solutions and the PDE simulation where the dilute approximation is no longer valid will be carried out in section 6.2. There, we show that the estimates from the phase space analysis for the DAE system (5.3)-(5.4) can be used to investigate the structure observed in Fig. 3 (set 2). In addition, for parameter set 1, a comparison of the results from the DAE system (5.3)-(5.4) and the PDE simulations is given in the supplemental notes, section SM4.

6. Spinodal decomposition. In the previous section we have seen how changing the properties of the bath can be sufficient to induce phase separation of the gel via development and propagation of a depletion front. In this section we are interested in another common modality of phase separation: spinodal decomposition. In this scenario, a spatially homogeneous region of the gel spontaneously separates into regions of high and low solvent content once perturbed with noise. This can occur when the homogeneous state the gel is in is unstable. As discussed in [15], spinodal decomposition can be induced in neutral gels by changing the temperature T and hence the parameter χ . While we will also discuss this scenario briefly (see Fig. 12), for the polyelectrolyte gels studied here, we examine whether spinodal decomposition can also be induced by changing the ion concentration in the bath.

6.1. Stability analysis. As shown in Fig. 3, the transition between different equilibrium states can also be accompanied by phase separation via spinodal decomposition of the gel bulk (region ahead of the front). To understand this mechanism, we investigate the stability of the initial homogeneous composition of the gel bulk, here denoted by $(\bar{\phi}_s, \bar{\phi}_+)$, to small amplitude perturbations. As in Section 5.1, we rescale z with ω , which is the characteristic length scale of the internal interfaces; to ease the algebra we further scale t with ω^{-1} . Since ω is small, the homogeneous region of the gel now fills the entire space $-\infty < z < \infty$.

We can now perturb the base state $(\bar{\phi}_s, \bar{\phi}_+)$ with normal modes suitable for an infinite domain by letting

$$(6.1) \quad \phi_s = \bar{\phi}_s + \delta \tilde{\phi}_s e^{ikz + \lambda t}, \quad \phi_+ = \bar{\phi}_+ + \delta \tilde{\phi}_+ e^{ikz + \lambda t}$$

with $k \in \mathbb{R}$, $\delta \ll 1$, and $\lambda \in \mathbb{C}$ being the wavenumber, amplitude, and growth rate of the perturbation. Substituting (6.1) into the governing equations (3.9)-(3.10) and keeping only the $O(\delta)$ terms leads to the 2×2 system

$$(6.2a) \quad \lambda \tilde{\phi}_s + k^2 [(1 - \bar{\phi}_s) \tilde{j}_s - 2\bar{\phi}_s \tilde{j}_+] = 0,$$

$$(6.2b) \quad \lambda \tilde{\phi}_+ + k^2 [(1 - 2\bar{\phi}_+) \tilde{j}_+ - \bar{\phi}_+ \tilde{j}_s] = 0,$$

where \tilde{j}_s and \tilde{j}_+ are the solution of the linear system

$$(6.2c) \quad \left(1 + \frac{\alpha_f \bar{\phi}_n}{\mathcal{D} \bar{\phi}_s}\right) \tilde{j}_s - \frac{\alpha_f \bar{\phi}_n}{\mathcal{D} \bar{\phi}_-} \tilde{j}_+ = \left[(\bar{\phi}_s B_{\phi_+} + \bar{\phi}_+ A_{\phi_+}) \tilde{\phi}_+ + (k^2 \bar{\phi}_s (1 + \alpha_f) \bar{\phi}_n + \bar{\phi}_s B_{\phi_s} + \bar{\phi}_+ A_{\phi_s}) \tilde{\phi}_s\right]$$

$$(6.2d) \quad \left(1 + \frac{\bar{\phi}_+}{\bar{\phi}_-}\right) \tilde{j}_+ - \frac{2\bar{\phi}_+}{\bar{\phi}_s} \tilde{j}_s = \mathcal{D} \bar{\phi}_+ \left[(A_{\phi_+} - 2k^2 \bar{\phi}_s) \tilde{\phi}_s + A_{\phi_+} \tilde{\phi}_+\right].$$

The subscripts ϕ_s, ϕ_+ now denote the derivatives of A and B with respect to these variables evaluated at $(\bar{\phi}_s, \bar{\phi}_+)$. The values of $\bar{\phi}_-$ and $\bar{\phi}_n$ are defined by evaluating (3.10f)-(3.10g) at $\bar{\phi}_s, \bar{\phi}_+$. Note that we could have solved explicitly for \tilde{j}_s and

594 \tilde{j}_+ but this would not benefit the exposition given the complexity of the equations.
 595 Imposing that the system (6.2) has non-trivial solution, we obtain the growth rate
 596 $\lambda = \lambda(k)$ as the roots of the characteristic polynomial:

$$597 \quad (6.3) \quad P_k(\lambda) = \lambda^2 + \frac{\zeta_{20} + \zeta_{22}k^2}{\zeta_1}k^2\lambda + \frac{\zeta_{30} + \zeta_{32}k^2}{\zeta_1}k^4\mathcal{D},$$

598 where the relevant coefficients ζ are functions of $(\bar{\phi}_s, \bar{\phi}_+)$ (see supplemental material,
 599 section SM3) and $\zeta_1 > 0$. The two roots of (6.3) are

$$600 \quad (6.4a) \quad \lambda_{\pm}(k) = \frac{1}{2} \left[\mathcal{T}_k \pm \sqrt{\mathcal{T}_k^2 - 4\Delta_k} \right],$$

$$601 \quad (6.4b) \quad \mathcal{T}_k = -\frac{\zeta_{20} + \zeta_{22}k^2}{\zeta_1}k^2, \quad \Delta_k = \frac{\zeta_{30} + \zeta_{32}k^2}{\zeta_1}k^4\mathcal{D}.$$

603 The homogeneous state is stable if and only if the real part of $\lambda_{\pm}(k)$ is negative for
 604 all k . We note that $\lambda_{\pm}(k)$ are equivalent to the eigenvalues of the linear dynamical
 605 system $\dot{\mathbf{y}} = A_k \mathbf{y}$, where $\mathbf{y} \in \mathbb{R}^2$ and $A_k \in \mathbb{R}^{2 \times 2}$ has trace \mathcal{T}_k and determinant Δ_k . We
 606 will refer to this class of dynamical systems, which is parametrised by k , as Σ_k . The
 607 problem of studying the stability of the mode k is therefore analogous to studying the
 608 stability of $(0, 0)$ for the system Σ_k . We therefore have that the k -th mode is stable if
 609 and only if $\mathcal{T}_k < 0$ and $\Delta_k > 0$. When considering $k \gg 1$ then $\Delta_k \approx \mathcal{D}k^6\zeta_{32}/\zeta_1$ and
 610 $\mathcal{T}_k \approx -\zeta_{22}k^4/\zeta_1$. Since ζ_1, ζ_{22} and ζ_{32} are always positive the conditions of stability
 611 are always satisfied for large wavenumbers. This implies that $(\bar{\phi}_s, \bar{\phi}_+)$ is unstable if
 612 and only if the system Σ_k has at least a bifurcation point $k_* > 0$, where the stability
 613 of $\mathbf{y} = (0, 0)$ changes. If Σ_k has no bifurcation point, then $(\bar{\phi}_s, \bar{\phi}_+)$ is stable. Let us
 614 assume such $k_* > 0$ exist then

$$615 \quad (6.5a) \quad \text{either } \Delta_{k_*} = 0 \text{ and } \mathcal{T}_{k_*} \leq 0,$$

$$616 \quad (6.5b) \quad \text{or } \Delta_{k_*} \geq 0 \text{ and } \mathcal{T}_{k_*} = 0,$$

618 where (6.5a) corresponds to $(0, 0)$ switching from a saddle to a stable node, while (6.5a)
 619 corresponds to a transition from an unstable to a stable spiral. The first scenario
 620 can occur only if $\zeta_{30} < 0$ and $\zeta_{30}\zeta_{22} - \zeta_{20}\zeta_{32} \leq 0$ (condition 1), while the second
 621 only if $\zeta_{20} < 0$ and $\zeta_{30}\zeta_{22} - \zeta_{20}\zeta_{32} \geq 0$ (condition 2). If we denote by \mathcal{S}_- the set
 622 of unstable homogeneous states, this is given by the union of the subsets of states
 623 satisfying condition 1 or 2. Manipulating the given inequalities, we find that the
 624 condition on $\zeta_{30}\zeta_{22} - \zeta_{20}\zeta_{32}$ does not actually play a role in determining the stability
 625 of a homogenous state and \mathcal{S}_- is given by

$$626 \quad (6.6) \quad \mathcal{S}_- = \{(\bar{\phi}_s, \bar{\phi}_+) \in (0, 1)^2, \text{ s.t. } \zeta_{30}(\bar{\phi}_s, \bar{\phi}_+) < 0 \text{ or } \zeta_{20}(\bar{\phi}_s, \bar{\phi}_+) < 0\}.$$

627 The spinodal curve, which delimits the region of stability is therefore

$$628 \quad (6.7) \quad \partial\mathcal{S} = \{(\bar{\phi}_s, \bar{\phi}_+) \in (0, 1)^2, \text{ s.t. } \zeta_{30}(\bar{\phi}_s, \bar{\phi}_+) = 0 \text{ \& } \zeta_{20}(\bar{\phi}_s, \bar{\phi}_+) \geq 0\} \\ \bigcup \{(\bar{\phi}_s, \bar{\phi}_+) \in (0, 1)^2, \text{ s.t. } \zeta_{30}(\bar{\phi}_s, \bar{\phi}_+) \geq 0 \text{ \& } \zeta_{20}(\bar{\phi}_s, \bar{\phi}_+) = 0\}.$$

629 **6.1.1. The limit of dilute salt concentration.** Let us define $\bar{\phi}_+ = \alpha_f \epsilon^2 \tilde{\phi}_+$
 630 (as in section 5.1) and take the limit $\epsilon \rightarrow 0$. Reasoning as in the previous section
 631 (more details in section SM3.1 of supplemental material), we obtain that the stability

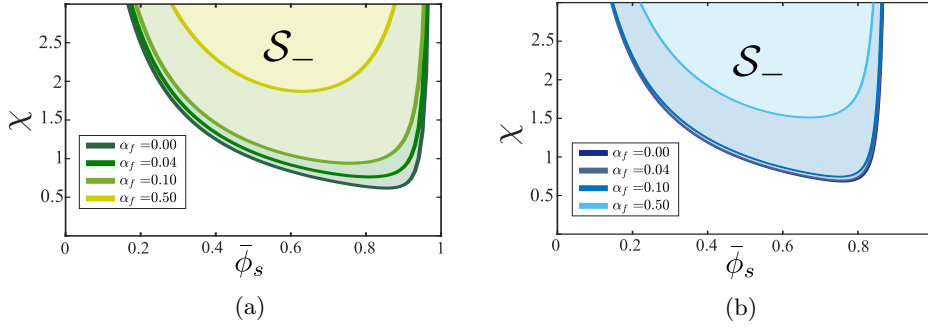


Fig. 10: Effect of the fixed charges on the stability region of an homogenous steady state for (a) dilute salt solution (b) non-dilute solution ($\bar{\phi}_+ = 0.05$). We highlight with colour the instability region \mathcal{S}_- which is the region contained in the curve $\partial\mathcal{S}$. In both plots, \mathcal{G} is set to its default given in Eqs. (3.13a).

of the system is governed by the leading order approximation of the coefficients $\zeta_{20}^{(0)}$ and $\zeta_{30}^{(0)}$ which are of the form:

$$(6.8) \quad \zeta_{20}^{(0)} = \frac{(\bar{\phi}_n^{(0)})^{-1}}{1 + \alpha_f} \left(B_{\phi_s}^{(0)} \bar{\phi}_s (1 - \bar{\phi}_s) + [\mathcal{D} + \alpha_f \bar{\phi}_s^{-1} \bar{\phi}_n^{(0)}] \right), \quad \zeta_{30}^{(0)} = \bar{\phi}_s B_{\phi_s}^{(0)},$$

where $B_{\phi_s}^{(0)} = B_{\phi_s}^{(0)}(\bar{\phi}_s)$ only depends on the concentration of the solvent. It is therefore apparent that when $\zeta_{20}^{(0)} = 0$ then $\zeta_{30}^{(0)} < 0$, while whenever $\zeta_{30}^{(0)} = 0$ then $\zeta_{20}^{(0)} > 0$. Consequently, the spinoidal curve $\partial\mathcal{S}$ as in (6.7) reduces to:

$$(6.9a) \quad \partial\mathcal{S} = \left\{ \bar{\phi}_s \in (0, 1), \text{ s.t. } B_{\phi_s}^{(0)}(\bar{\phi}_s) = 0 \right\},$$

where

$$(6.9b) \quad B_{\phi_s}^{(0)}(\bar{\phi}_s) = \bar{\phi}_s^{-1} - \frac{[1 + 2\chi(1 - \bar{\phi}_s)]}{1 + \alpha_f} + \frac{\mathcal{G}}{1 + \alpha_f} \left[1 + \left(\frac{1 + \alpha_f}{1 - \bar{\phi}_s} \right)^2 \right].$$

As discussed in the supplemental material, Section SM3.1, Equation (6.9) still holds for $\alpha_f \rightarrow 0$. Furthermore, setting $\alpha_f = 0$, we retrieve the same result as in [15] for phase separation in neutral hydrogels (i.e. gel with no fixed charge on the polymer network). As shown in Fig. 10a, as we increase α_f , the domain \mathcal{S}_- shrinks which mean higher concentration of fixed charges on the polymer network can stabilise the system. Small perturbations of the homogeneous state will generate an electric field that tends to re-distribute charges homogeneously. As the number of fixed charges in the network increases so does the strength of the electric field resulting in the stabilisation of homogeneous states. As shown in Fig. 10b, we can see a similar trend also for the non-dilute limit (more details in the following section). Fixed charges tend again to stabilise the system, however, for larger $\bar{\phi}_+$ the shrinking of the unstable region \mathcal{S}_- is less than in the dilute scenario.

6.1.2. The general case. Let us now go back to the general case of a non-dilute solutions. For the reference parameter values in (3.13), we have that $\zeta_{20}(\bar{\phi}_s, \bar{\phi}_+)$ is always positive. This implies that the transition to instability can only occur via a

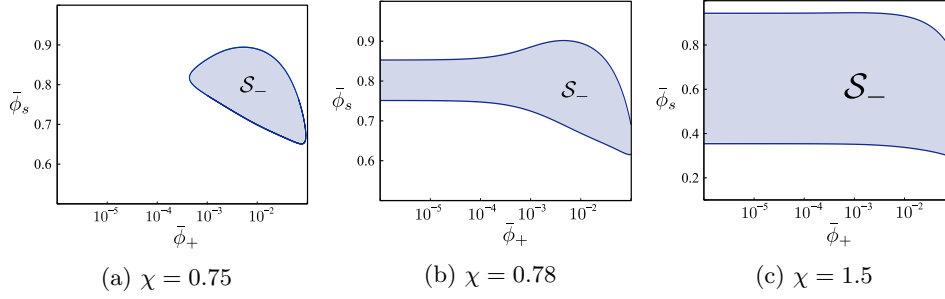


Fig. 11: Plots of the instability region \mathcal{S}_- (as defined by Eq. (6.6)) for increasing values of χ . Parameters α_f and \mathcal{G} are set to their default given in Eqs. (3.13a).

saddle-node bifurcation. Hence $\partial\mathcal{S}$ is implicitly defined by $\zeta_{30}(\bar{\phi}_s, \bar{\phi}_+) = 0$ which can be computed via numerical continuation. As shown in Fig. 11, for concentrations $\bar{\phi}_+ < 10^{-4}$, the shape and size of the domain \mathcal{S}_- is independent of the actual value of $\bar{\phi}_+$, in line with the result from the dilute analysis in section 5.1. As we move away from the dilute limit by increasing $\bar{\phi}_+$, two scenarios are possible. If χ is sufficiently small (as in Fig. 11a-11b), then the size of \mathcal{S}_- tends to increase with $\bar{\phi}_+$. This is particularly evident in Fig. 11a, where in the dilute regime all homogenous states are stable, and the system only allows for spinodal decomposition to occur in the non-dilute regime, i.e. $\bar{\phi}_+ \approx 10^{-3}$. If we are however to increase $\bar{\phi}_+$ further (i.e. $\bar{\phi}_+ \approx 10^{-2}$) then \mathcal{S}_- starts to shrink and the unstable state corresponds to a less swollen gel. If χ is chosen to be even larger (such as Fig. 11c), then increasing $\bar{\phi}_+$ only results in the shrinking of the instability region. We note that Fig. 11b is generated using the default parameter values used in the paper and given in Eqs. (3.13a); consequently the spinodal region in Fig. 11b is the same one presented in Figs. 3, 4a and 13. Furthermore, the linear stability analysis reveals that the parameter ω , related to the interfacial energy, does not influence the boundary of the region of linear stability for the system (both in the dilute and non-dilute case). However, the larger ω is, the smaller the value of largest unstable mode k_* is, where $k_* \rightarrow \infty$ as $\omega \rightarrow 0$. The initial development of instability will be thus driven by the mode $k < k_*$ corresponding to the largest positive growth rate $\lambda(k)$. Therefore, ω does not determine (in the limit where ω is small compared to the size of the gel) whether spinodal decomposition occurs or not, but it can impact the spatial patterns that emerge as a result of instability.

Based on stability analysis, we now want to identify how we can drive spinodal decomposition in a gel. A standard approach is to increase the value of χ (i.e the temperature) [15]. This exploits the fact that size of the domain \mathcal{S}_- increases with χ and moving along a vertical line in Fig. 10 can push the system into the unstable regime. We explore this scenario numerically, by considering an initially homogeneous gel in equilibrium with an ionic bath (parameter values $\phi_0 = 5 \times 10^{-3}$ and $\chi = 0.78$). At time $t = 0$, the gel is isolated and the temperature is raised so that χ increases to $\chi = 1.2$. As shown in the phase plane in Fig. 12 this is sufficient to move the system from the stable region (see the red point in the phase plane of Fig. 12) into the unstable regime (see the green point in the phase plane of Fig. 12). As we introduced some noise in the system, growing perturbations rapidly fill the entire length of the gel and then begin to coarsen or collide, resulting in fewer and broader spikes. As shown in the phase plane in Fig. 12, the peak (point P) and trough (point Q) of the spikes are

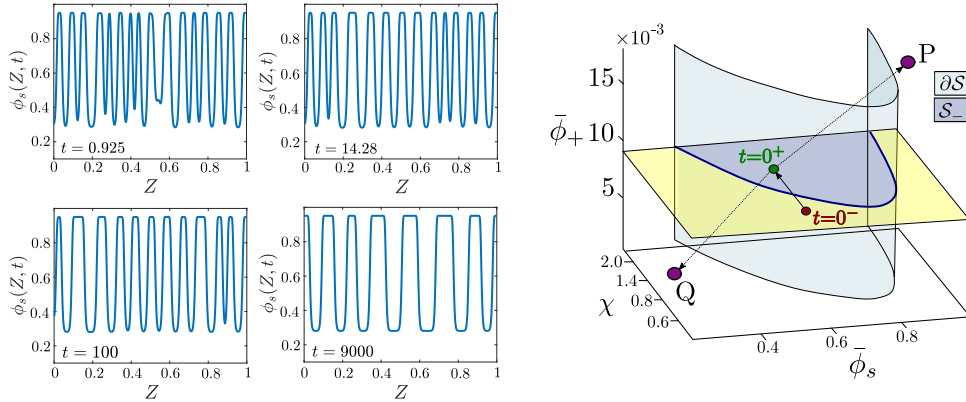


Fig. 12: Spinodal decomposition in an isolated gel. Initially (see red point in the phase plane) the gel is equilibrated with a bath ($\phi_{0-} = 5 \times 10^{-3}$). At time $t = 0$, we isolate the gel, increase χ from 0.78 to 1.2 (see green point in the phase plane) and introduce some noise. On the left, we illustrate the evolution of the ϕ_s approximated solving numerically Eqs. (3.9)-(3.10) with boundary conditions (3.12); on the right, we identify the manifold $\partial\mathcal{S}$ that divides the stable (yellow) and unstable (blue) region. The point P and Q represent the peak and the trough of the spikes. We use the values $\mathcal{G} = 0.001$, $\omega = 0.01$, $\alpha_f = 0.04$ and $\mathcal{D} = 5$.

located in the region of linear stability. Hence, no further instabilities develop. Over time, the evolution slows down until the pattern is almost stationary. However, we expect that in principle coarsening continues until only two regions remain, one in the collapsed state with $\phi_s \approx 0.3$ and the other in the swollen state with $\phi_s \approx 0.9$. These two end-state values are stable as indicated in the right-most panel in the figure.

6.2. Spinodal decomposition of a collapsing gel. The stability analysis however hints at another possible mechanism to drive spinodal decomposition in polyelectrolyte gels: increasing the concentration of co-ions in the system. Experimentally, this can be achieved maintaining the gel in contact with the bath and increasing ϕ_0 . As discussed in Section 5, the ions rapidly diffuse in the gel bulk while the solvent concentration remains constant in this fast transient. Exploiting the different time scales in the system, we can therefore move along horizontal lines in the phase plane of Fig. 11. For $\chi = 0.78$ (as in the simulation in Section 5), changes in the instability region \mathcal{S}_- occur only when $\phi_+ \sim O(10^{-3})$. Using the equation (5.2), we obtain that ϕ_{0+} must be increased to $\phi_{0+} \sim O(10^{-2})$ in order to exploit the growth of \mathcal{S}_- .

An example of this scenario is shown in Fig. 13, where we present the results of the numerical simulation for set 2 in (3.13). As expected the ions rapidly diffuse in the gel, driving the bulk of the gel into the unstable region of the phase diagram; see $t = 26$ in the right panel of Fig. 13. This results in the onset of spinodal decomposition, which give rise to a series of solvent-depleted phases, which coarsen and collide first rapidly and then very slowly. Interestingly, at the centre of each region with a low solvent concentration there is also a high counter-ion (ϕ_-) concentration, as a consequence of maintaining electro-neutrality (see Fig. 14). As shown in Fig. 13, on a longer time scale, the depletion front propagates into the gel, consuming the array of solvent-depleted domains. When comparing with the result in Fig. 5, we note that the front

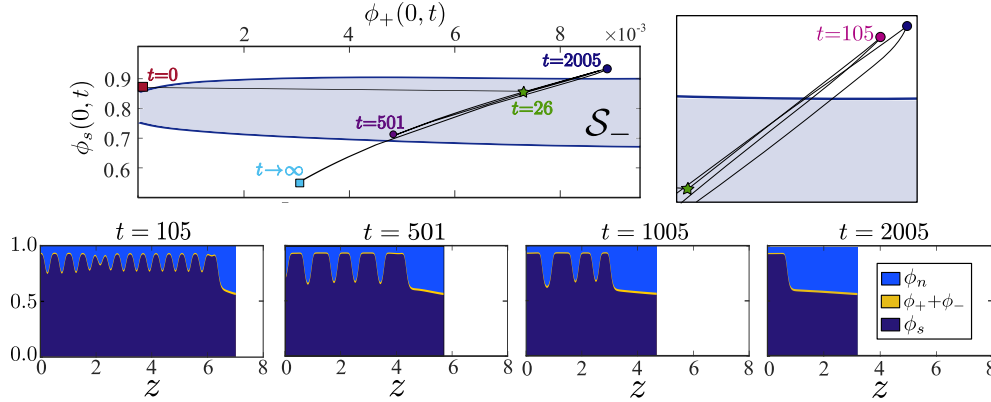


Fig. 13: Spinodal decomposition in a collapsing gel: (top) time evolution of the gel composition (ϕ_s, ϕ_+) at location $z = 0$. The instability region \mathcal{S}_- as predicted by the stability analysis is highlighted in blue (details on how this is compute given in Section 6.1.2); the panel on the right is a zoom near the green star and the blue dot to better visualise the complexity of the trajectories; (bottom) snapshot of the gel composition at different time points approximated solving numerically Eqs. (3.9)-(3.11) with parameter values corresponding to set 2 in (3.13).

propagates faster in this case, with spinodal decomposition facilitating the removal of solvent from the gel.

Again, we can use the phase-plane analysis (see Sec. 5.1) for (5.3)-(5.4) to predict the structure of the collapsing gel. In doing so, we set $\tilde{\mu} = 0$ since, numerically, we find that $|\tilde{\mu}| < 10^{-3} \ll \ln \alpha_f \epsilon$. When considering the depletion front, the full model and the phase-space analysis deviate slightly. As shown in Fig. 14, the front obtained via the phase-plane analysis is too steep and its lower limit does not capture the actual right state of the front very well. The interface of the solvent-depleted sub-domains forming in the bulk of the gel yields a better comparison with a homoclinic orbit. The value of μ_s was chosen so that the minimum value for ϕ_s matches the local minimum for the PDE simulations next to the depletion front (see first panel in the figure). The homoclinic orbit matches the PDE simulations almost perfectly for all three variables displayed in the panels. A possible explanation of the higher discrepancy is that the front evolves more rapidly so that the quasi-stationary assumption underlying the phase plane analysis breaks down. This is located near the free interface, where we have larger variations in the chemical potentials and therefore fluxes so that the quasi-stationary assumption underlying the phase-plane analysis may not hold.

7. Conclusions. In this study we have focussed on the transient dynamics of a polyelectrolyte gel in contact with a ionic bath containing a monovalent salt. Starting from a homogeneous equilibrium, we initiate the collapse of the gel by changing the surrounding salt concentration. Depending on the properties of the system, temporary patterns form with highly swollen and collapsed regions can co-existing in the gel. Using the phase-field model developed in the companion paper [4], we can track the evolution of these internal interfaces, delineating the regions where the gel network has collapsed after they have formed via phase separation. We here consider the

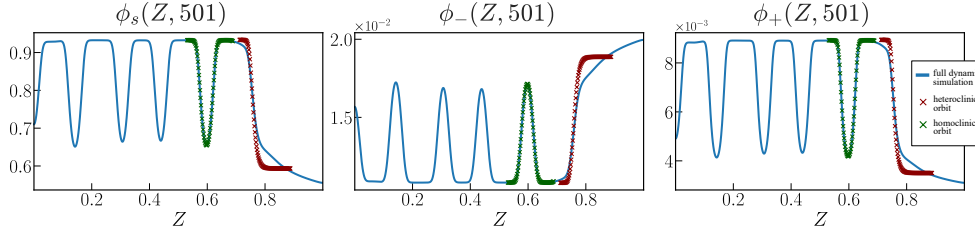


Fig. 14: Comparison of the phase plane solution and the numerical values of ϕ_s , ϕ_- and ϕ_+ at time $t = 501$ estimated from the full dynamical simulation (same parameter values as Fig. 13). We compare the front from the solution of the simulation of the full system (blue curve) with the approximated heteroclinic orbit for Eqs. (5.3). The downward spikes are instead compared with the approximated homoclinic orbit (green crosses) for Eqs. (5.3). Details on the computations can be found in Section 5.1.2

case of a one-dimensional constrained geometry, with a single free interface in contact with the bath. The model is further simplified by passing to the electroneutral limit, justified by the infinitesimal size of the electric double layer compared to the other spatial scales in the model.

Depending on the value of various model parameters, such as the Flory interaction parameter χ , the gel shear modulus \mathcal{G} , and the ratio of the salt concentration in the bath and the fixed charges on the polymer network $\epsilon = \phi_0/\alpha_f$, the stability properties of the homogeneous states vary. Our numerical results for the case where the gel is isolated from the bath (by using no-flux boundary conditions at the free interface) show that as the unstable homogeneous state undergoes spinodal decomposition, it forms arrays of locally collapsed solvent-depleted domains with a high concentrations of counter-ions. These eventually coarsen into a new stable equilibrium.

When in contact with the bath, the gel is sensitive to the salt concentration ϕ_0 in the surrounding fluid. Increasing ϕ_0 initiates and drives the collapse of the gel. This process is characterised by a depletion front that forms via phase separation and travels into the gel. Using phase-plane analysis, we are able to show that the depletion front selects the homogeneous states at its front and rear. These are always linearly stable. In the spinodally unstable regime, the emerging structure of collapsed solvent-depleted domains are well approximated by homoclinic solutions of the DAE system, and are consumed by the depletion front that propagates through the gel on a faster time scale than the coarsening process.

Even though our analysis is currently only one-dimensional, it sheds light on the possibility of observing these patterns experimentally. Depending on parameter settings, the transient patterns with high concentration of ϕ_- in the collapsed and high concentration of ϕ_+ in the swollen regions are in principle observable. Our approach provides a template for how mathematical techniques such as the phase-plane analysis and stability analysis can elucidate the notoriously complicated models for polyelectrolytes, beyond numerical simulations, particularly when employed in combination.

An important consequence of our approach is that fundamental quantities, such as the velocity of the localised front, can now be predicted using an asymptotic analysis based on our approximation of the depletion front. Our analysis can also be easily generalised to settings that account for example for multivalent salts and concentration-

Acknowledgments. MH recognizes support from the Mathematical Institute through a Hooke fellowship, and GC acknowledges the EPSRC and MRC Centre for Doctoral Training in Systems Approaches to Biomedical Science and Cancer Research UK for funding.

784

- 785
786
787
788
789
790
791
792
793
794
795
796
797
798
799
800
801
802
803
804
805
806
807
808
809
810
811
812
813
814
815
816
817
818
819
820
821
822
823
824
825
826
827
828
829
830
831
832
833

- [19] J. HUA, M. K. MITRA, AND M. MUTHUKUMAR, *Theory of volume transition in polyelectrolyte gels with charge regularization*, The Journal of Chemical Physics, 136 (2012), p. 134901, <https://doi.org/10.1063/1.3698168>.
- [20] J. M. HUYGHE AND J. D. JANSSEN, *Quadruphasic mechanics of swelling incompressible porous media*, International Journal of Engineering Science, 35 (1997), pp. 793–802, [https://doi.org/10.1016/S0020-7225\(96\)00119-X](https://doi.org/10.1016/S0020-7225(96)00119-X).
- [21] A. R. KHOKHLOV AND E. Y. KRAMARENKO, *Weakly charged polyelectrolytes: collapse induced by extra ionization*, Macromolecules, 29 (1996), pp. 681–685, <https://doi.org/10.1021/ma946426d>.
- [22] E. KOKUFUTA, *Polyelectrolyte gel transitions: experimental aspects of charge inhomogeneity in the swelling and segmental attractions in the shrinking*, Langmuir, 21 (2005), pp. 10004–10015, <https://doi.org/10.1021/la050530e>.
- [23] H. J. KWON, Y. OSADA, AND J. P. GONG, *Polyelectrolyte gels-fundamentals and applications*, Polymer Journal, 38 (2006), pp. 1211–1219, <https://doi.org/10.1295/polymj.PJ2006125>.
- [24] O. LEWIS, J. KEENER, AND A. FOGELSON, *Electrodifusion-Mediated Swelling of a Two-Phase Gel Model of Gastric Mucus*, Gels, 4 (2018), p. 76, <https://doi.org/10.3390/gels4030076>.
- [25] M. P. LUTOLF AND J. A. HUBBELL, *Synthetic biomaterials as instructive extracellular microenvironments for morphogenesis in tissue engineering*, jan 2005, <https://doi.org/10.1038/nbt1055>.
- [26] E. S. MATSUO AND T. TANAKA, *Patterns in shrinking gels*, Nature, 358 (1992), pp. 482–485, <https://doi.org/10.1038/358482a0>.
- [27] J. L. MCCOY AND M. MUTHUKUMAR, *Dynamic light scattering studies of ionic and nonionic polymer gels with continuous and discontinuous volume transitions*, Journal of Polymer Science Part B: Polymer Physics, 48 (2010), pp. 2193–2206, <https://doi.org/10.1002/polb.22101>.
- [28] Y. MORI, H. CHEN, C. MICEK, AND M.-C. CALDERER, *A dynamic model of polyelectrolyte gels*, SIAM Journal on Applied Mathematics, 73 (2013), pp. 104–133.
- [29] M. MUSSEL AND F. HORKAY, *Experimental Evidence for Universal Behavior of Ion-Induced Volume Phase Transition in Sodium Polyacrylate Gels*, The Journal of Physical Chemistry Letters, 10 (2019), pp. 7831–7835, <https://doi.org/10.1021/acs.jpclett.9b03126>.
- [30] C. NING, Z. ZHOU, G. TAN, Y. ZHU, AND C. MAO, *Electroactive polymers for tissue regeneration: Developments and perspectives*, jun 2018, <https://doi.org/10.1016/j.progpolymsci.2018.01.001>.
- [31] S. PURI AND K. BINDER, *Surface-directed phase separation with off-critical composition: Analytical and numerical results*, Physical Review E, 66 (2002), p. 061602, <https://doi.org/10.1103/PhysRevE.66.061602>.
- [32] D. ROSHAL, O. KONEVTSOVA, A. LOSDORFER BOZIC, AND ET AL., *ph-induced morphological changes of proteinaceous viral shells*, Scientific Reports, 9 (2019), p. 5341, <https://doi.org/10.1038/s41598-019-41799-6>.
- [33] E. SATO MATSUO AND T. TANAKA, *Kinetics of discontinuous volume-phase transition of gels*, The Journal of Chemical Physics, 89 (1988), pp. 1695–1703.
- [34] T. K. SHERWOOD, R. L. PIGFORD, AND C. R. WILKE, *Mass transfer*, McGraw-Hill Book Co, New York, 1975.
- [35] C. E. SING, J. W. ZWANIKKEN, AND M. OLVERA DE LA CRUZ, *Effect of ion-ion correlations on polyelectrolyte gel collapse and reentrant swelling*, Macromolecules, 46 (2013), pp. 5053–5065, <https://doi.org/10.1021/ma400372p>.
- [36] S. SIRCAR, J. P. KEENER, AND A. L. FOGELSON, *The effect of divalent vs. monovalent ions on the swelling of Mucin-like polyelectrolyte gels: Governing equations and equilibrium analysis*, The Journal of Chemical Physics, 138 (2013), p. 014901, <https://doi.org/10.1063/1.4772405>.
- [37] M. A. STUART, W. T. HUCK, J. GENZER, M. MÜLLER, C. OBER, M. STAMM, G. B. SUKHORUKOV, I. SZLEIFER, V. V. TSUKRUK, M. URBAN, F. WINNIK, S. ZAUSCHER, I. LUZINOV, AND S. MINKO, *Emerging applications of stimuli-responsive polymer materials*, Nature Materials, 9 (2010), pp. 101–113, <https://doi.org/10.1038/nmat2614>.
- [38] T. TANAKA, *Collapse of gels and the critical endpoint*, Phys. Rev. Lett., 40 (1978), pp. 820–823, <https://doi.org/10.1103/PhysRevLett.40.820>, <https://link.aps.org/doi/10.1103/PhysRevLett.40.820>.
- [39] T. TOMARI AND M. DOI, *Hysteresis and incubation in the dynamics of volume transition of spherical gels*, Macromolecules, 28 (1995), pp. 8334–8343.
- [40] Y. YU, C. M. LANDIS, AND R. HUANG, *Salt-induced swelling and volume phase transition of polyelectrolyte gels*, Journal of Applied Mechanics, 84 (2017), p. 051005, <https://doi.org/10.1115/1.4036113>.

- 896 [41] R. ZANDI, B. DRAGNEA, A. TRAVESSET, AND R. PODGORNIK, *On virus growth and form*, Physics
897 Reports, 847 (2020), pp. 1–102, <https://doi.org/10.1016/j.physrep.2019.12.005>.
898 [42] A. Y. ZUBAREV, F. A. BLYAKHMAN, G. H. POLLACK, P. GUSEV, AND A. P. SAFRONOV, *Self-*
899 *Similar Wave of Swelling/Collapse Phase Transition along Polyelectrolyte Gel*, Macro-
900 molecular Theory and Simulations, 13 (2004), pp. 697–701, [https://doi.org/10.1002/mats.](https://doi.org/10.1002/mats.200400027)
901 [200400027](https://doi.org/10.1002/mats.200400027).